

Splitting horizontal and vertical polynomial order in a compatible finite element discretisation for numerical weather prediction

Daniel Witt^{1*}

Jemma Shipton¹

Thomas M Bendall²

¹Department of Mathematics, University of Exeter, Exeter, United Kingdom

²Dynamics Research, UK Met Office, Exeter, United Kingdom

1 Abstract

The accurate and efficient representation of atmospheric dynamics remains a central challenge in numerical weather prediction. A particular difficulty arises from the strong anisotropy of the atmosphere, in which horizontal and vertical motions occur on very different length scales, motivating numerical discretisations that can reflect this structure. In this study, we introduce a compatible finite element discretisation of the compressible Boussinesq and compressible Euler equations in which the horizontal and vertical polynomial orders are treated independently.

The split-order discretisation is constructed using a tensor-product framework that preserves the discrete de Rham complex and associated mimetic properties. Its wave-propagation characteristics are examined through a discrete dispersion analysis that extends previous analyses to configurations with differing horizontal and vertical polynomial orders. The results show that increasing horizontal order improves the representation of gravity waves at low and intermediate wavenumbers, while increasing vertical order can degrade dispersion accuracy near the grid scale and introduce spectral gaps.

A series of idealised numerical experiments, including gravity-wave propagation, advective transport, mountain-wave flow, and a global baroclinic-wave test, is used to assess the scheme's accuracy and convergence properties. These experiments demonstrate that increasing the polynomial order in the dominant direction of motion improves convergence, and that increasing the horizontal order yields the greatest gain in accuracy under typical atmospheric conditions. The results indicate that split-order compatible finite element discretisations provide a viable alternative for controlling accuracy and numerical behaviour in atmospheric dynamical cores.

*Corresponding author: D.witt@exeter.ac.uk

2 Introduction

The UK Met Office has developed a new dynamical core, LFRic, which uses a compatible finite-element discretisation (Adams *et al.*, 2019; Melvin *et al.*, 2024, 2019) that preserves many of the desirable properties of the Met Office’s previous ENDGame dynamical core (Wood *et al.*, 2014; Melvin *et al.*, 2010). ENDGame is a semi-implicit semi-Lagrangian finite difference model discretised on a latitude-longitude grid, with Arakawa C-grid and Charney-Phillips staggerings (Arakawa and Lamb, 1977; Charney and Phillips, 1953). This discretisation choice ensures that ENDGame has good wave dispersion properties and avoids spurious pressure modes, which Staniforth and Thuburn (2012) identify as necessary and desirable features for a dynamical core. These features ensure that the dynamical core correctly captures wave propagation and key atmospheric features, such as geostrophic balance, without resorting to numerical diffusion to suppress computational noise. Despite these desirable properties, ENDGame’s reliance on a latitude-longitude grid poses a significant hurdle with the increasingly parallel architecture of modern supercomputers; higher-resolution latitude-longitude grids create a communication bottleneck due to the clustering of grid cells at the poles. Compatible finite element methods retain the desirable wave-propagation properties and eliminate spurious pressure modes whilst also facilitating non-orthogonal quasi-uniform grids that circumvent the pole-clustering problem (Cotter and Shipton, 2012; Cotter, 2023; Natale *et al.*, 2016; Cotter and Shipton, 2022). In finite element methods, increasing the polynomial order offers an alternative to increasing resolution to improve model accuracy. Resolved motions in a finite element scheme are determined not only by the grid resolution but also by the node distribution within an element, which is governed by the polynomial order. Unlike finite difference or finite volume schemes, which rely on larger stencils for higher-order representation (such as computing the pressure gradient), higher-order finite element methods simply increase the polynomial order of representation, without the increased cell-to-cell communication associated with larger stencils. Nair *et al.* (2009) demonstrated that higher-order finite elements still retain strong computational scaling in massively parallel architectures.

We construct two and three-dimensional finite element spaces by taking the tensor product of finite element spaces representing the horizontal discretisation with those representing the vertical (see section 4). Many finite element discretisations are constructed this way, including the compatible variety (Cotter and Thuburn, 2014; Arnold *et al.*, 2006). This tensor product construction provides a framework in which the horizontal and vertical orders can be changed independently. For example, Guerra and Ullrich (2016) developed a general spectral element scheme for the vertical coordinate, which used higher order vertical elements to eliminate stationary modes and maintain hydrostatic balance whilst keeping the horizontal order relatively coarse.

We are motivated to treat the horizontal and vertical directions separately due to the anisotropy of the atmosphere, where horizontal length scales are significantly larger than vertical ones. How motion at these scales is represented in numerical models is intrinsic to their accuracy and performance. [Skamarock *et al.* \(2019\)](#) showed that mesoscale-inertia gravity waves were particularly sensitive to the vertical resolution, assuming that the horizontal resolution was well resolved. These waves are crucial to the mesoscale KE spectrum in the stratosphere, which is especially important for high-resolution global forecasts. However, for coarser models, such as those used in ensemble or climate forecasts, a coarser vertical resolution is appropriate to better filter spurious flow features without seriously deforming the KE spectra ([Burgess *et al.*, 2013](#); [Waite and Snyder, 2009](#)). [Schmidt *et al.* \(2024\)](#) found results indicating that global storm-resolving models also benefited more from an increase in horizontal resolution than vertical resolution. It is therefore desirable that a model’s spatial discretisation remain flexible, allowing the best combination of vertical and horizontal orders to be chosen for the particular modelling goal. This can extend to the model construction; for instance, LFRic stores data in an unstructured manner in the horizontal direction but retains vertical structure by ensuring that vertically adjacent data points are adjacent in memory ([Adams *et al.*, 2019](#)). Therefore, changing the polynomial order in the vertical, not the horizontal, or vice versa, may have different effects on the balance between accuracy and computational performance.

Higher-order schemes offer greater accuracy; however, they also introduce new challenges. One such challenge is the degradation of numerical dispersion relations ([Le Roux *et al.*, 2007](#); [Melvin *et al.*, 2014](#); [Cotter, 2023](#)). Although compatible finite elements provide a good representation of the dispersion relation for low wavenumbers, there is a degradation at wavenumbers approaching the grid scale ([Melvin *et al.*, 2018](#); [Eldred and Le Roux, 2018](#)). Additionally, the higher-order node distribution within an element increases the resolved motions past the grid spacing; these resolved motions can exaggerate spurious numerical noise ([Herrington *et al.*, 2019](#); [Hannah *et al.*, 2021](#)). This motivates our discrete dispersion analysis to ensure that such degradations are either absent or minimal. When designing an operational dynamical core that must run within a fixed time window, we must balance attempts to improve accuracy with the resulting computational cost. In this work, we focus solely on the numerical behaviour of the split-order scheme, leaving questions of computational performance to future work.

In this paper, we develop and implement a novel split-order finite element scheme in Gusto, a compatible finite element dynamical core toolkit. To analyse its properties, we extend the dispersion analysis of [Melvin *et al.* \(2018\)](#) to cases with differing polynomial orders between the vertical and horizontal directions and complement this with a series of numerical experiments assessing the accuracy

of the resulting schemes. We show that the split-order discretisation improves dispersion behaviour at slow and intermediate wavenumbers but can degrade dispersion for wavenumbers approaching the grid scale. Increasing the polynomial order also introduces spectral gaps in the dispersion relation; however, we demonstrate that these do not affect numerical results in standard test cases. The paper is organised as follows: section 4 describes the construction of the split-order compatible finite element scheme. Section 5 presents a theoretical analysis of its dispersion properties. Section 6 outlines the numerical model and experimental setup. Results from test cases are shown in Section 7, followed by concluding remarks.

3 Governing equations

In this section, we introduce the equation sets we use in the rest of the paper. We use the compressible Boussinesq equations for a discrete dispersion analysis since this equation set has a linear pressure gradient term following (Melvin *et al.*, 2018, 2014). We use the compressible Euler equations to demonstrate the accuracy and convergence of the split-order method using standard tests commonly used in the development of weather and climate models.

3.1 Compressible Boussinesq equations

The compressible Boussinesq equations in a non-rotating domain are

$$\frac{\partial \mathbf{u}}{\partial t} + (\mathbf{u} \cdot \nabla) \mathbf{u} + \nabla p + b \hat{\mathbf{k}} = 0, \quad (1a)$$

$$\frac{\partial p}{\partial t} + (\mathbf{u} \cdot \nabla) p + c_s^2 \nabla \cdot \mathbf{u} = 0, \quad (1b)$$

$$\frac{\partial b}{\partial t} + (\mathbf{u} \cdot \nabla) b = 0, \quad (1c)$$

where \mathbf{u} is the velocity vector, p is the pressure, b is the buoyancy, $\hat{\mathbf{k}}$ is a unit vector in the vertical direction, and $c_s = 340 \text{ m s}^{-1}$ is the speed of sound.

3.2 Compressible Euler equations

The compressible Euler equations are

$$\frac{\partial \mathbf{u}}{\partial t} + (\mathbf{u} \cdot \nabla) \mathbf{u} + 2\boldsymbol{\Omega} \times \mathbf{u} + c_p \theta \nabla \Pi + g \hat{\mathbf{k}} = 0, \quad (2a)$$

$$\frac{\partial \rho}{\partial t} + \nabla \cdot (\mathbf{u} \rho) = 0, \quad (2b)$$

$$\frac{\partial \theta}{\partial t} + (\mathbf{u} \cdot \nabla) \theta = 0, \quad (2c)$$

$$\Pi^{(1-\kappa)/\kappa} = \frac{R}{p_0} \rho \theta, \quad (2d)$$

where \mathbf{u} is the velocity vector, θ is the potential temperature, ρ is the density, Π is the Exner pressure, c_p is the specific heat capacity at constant pressure, R is the gas constant, p_0 is the reference pressure, g is the acceleration due to gravity, $\kappa = R/c_p$, and $\boldsymbol{\Omega}$ is the planet's rotation vector.

4 Spatial Discretisation

As the numerical analysis in Section 5 uses the compressible Boussinesq equations, we present the discretisation of the linear compressible Boussinesq equations here. The discretisation of the compressible Euler equations follows the same method. Full details can be found in (Cotter and Shipton, 2022; Bendall and Wimmer, 2023). To discretise equation set (1) with compatible finite elements, we define a set of spaces in which to represent the prognostic variables (\mathbf{u}, p, b) and their corresponding test functions $(\boldsymbol{\psi}, \phi, \gamma)$. The spaces are chosen so that, together with the appropriate differential operators, they form a discrete de Rham complex; this ensures that our discretisation preserves the identities of continuous vector calculus. Preserving these identities ensures that spurious computational modes do not arise in the numerical solution and large-scale geostrophic flows are well represented (Natale *et al.*, 2016; Cotter and Shipton, 2012, 2022).

We construct two and three-dimensional finite element spaces by taking the tensor product between a horizontal finite element and a vertical finite element. The geometry of the domain determines the form of the horizontal space, an interval in two dimensions, or a quadrilateral or triangle in three dimensions. Many finite element spaces satisfy the de Rham conditions; however, here we use the sequence $(\mathbb{V}_1, \mathbb{V}_2)$ on quadrilateral cells, where \mathbb{V}_1 is an order r quadrilateral Raviart-Thomas element, which ensures continuity in the normal direction across the cell boundaries, and \mathbb{V}_2 is the required order $r - 1$ discontinuous space. The vertical element is always defined on an interval.

Figure 1 illustrates the continuous (CG_r^0) and discontinuous (DG_r^0) interval finite elements used for two-dimensional domains. Here, the superscript 0 indicates construction on an interval and r denotes

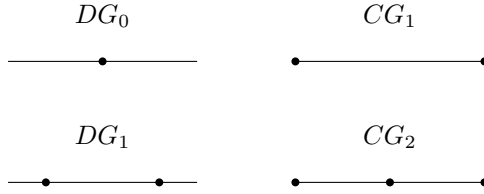


Figure 1: Diagrams of the one-dimensional finite element spaces used to build the two-dimensional spaces. Here, DG1 refers to discontinuous order 1 (linear) polynomials over the cell, CG2 continuous order 2 (quadratic) polynomials, etc. Dots represent degrees of freedom (DoF).

the polynomial order of the element.

In addition to the spaces that form the de Rham complex, we define another space, \mathbb{V}_b , with nodes co-located with the vertical velocity nodes, giving continuity in the vertical direction. We define the buoyancy variable in \mathbb{V}_b to mimic the Charney-Phillips grid staggering (Charney and Phillips, 1953; Melvin *et al.*, 2018, 2024; Bendall *et al.*, 2023). In this work, we consider a set of de Rham complexes with different horizontal and vertical order. These cases are denoted throughout by the tuple (h, v) , where h and v denote the horizontal and vertical orders in the \mathbb{V}_2 space, respectively. Our focus is on combinations of zeroth and first-order complexes, namely the cases $(0, 0)$, $(1, 0)$, $(0, 1)$, and $(1, 1)$, as illustrated in table 1. To construct these finite element spaces in a vertical slice, we take the following tensor products,

$$\mathbb{V}_2^{h,v} = DG_h^{0,x} \otimes DG_v^{0,z}, \quad (3a)$$

$$\mathbb{V}_1^{h,v} = CG_{h+1}^{0,x} \otimes DG_v^{0,z} + DG_h^{0,x} \otimes CG_{v+1}^{0,z}, \quad (3b)$$

$$\mathbb{V}_b^{h,v} = DG_h^{0,x} \otimes CG_{v+1}^{0,z}. \quad (3c)$$

Linearising equations (1a -1c) around a state of rest and multiplying each governing equation by a test function $(\psi, \phi, \gamma) \in \mathbb{V}_1 \times \mathbb{V}_2 \times \mathbb{V}_b$ then integrating over the domain Ω yields the spatial discretisation

$$\int_{\Omega} \frac{\partial u}{\partial t} \chi \, d\Omega - \int_{\Omega} p \frac{\partial \chi}{\partial x} \, d\Omega = 0, \quad \forall \chi \in \mathbb{V}_x, \quad (4a)$$

$$\int_{\Omega} \frac{\partial w}{\partial t} \nu \, d\Omega - \int_{\Omega} p \frac{\partial \nu}{\partial z} \, d\Omega - \int_{\Omega} b \nu \, d\Omega = 0, \quad \forall \nu \in \mathbb{V}_z, \quad (4b)$$

$$\int_{\Omega} \frac{\partial p}{\partial t} \psi \, d\Omega + c_s^2 \int_{\Omega} \left(\frac{\partial u}{\partial x} + \frac{\partial w}{\partial z} \right) \psi \, d\Omega = 0, \quad \forall \psi \in \mathbb{V}_2, \quad (4c)$$

$$\int_{\Omega} \frac{\partial b}{\partial t} \gamma \, d\Omega + \int_{\Omega} N^2 w \gamma \, d\Omega = 0, \quad \forall \gamma \in \mathbb{V}_b, \quad (4d)$$

where $\psi = (\chi, \nu)$. Here, we have separated the momentum equation into vertical and horizontal

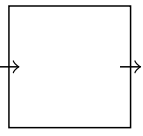
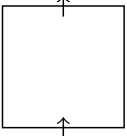
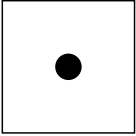
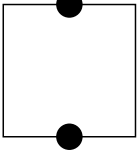
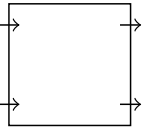
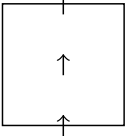
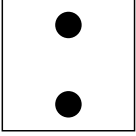
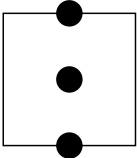
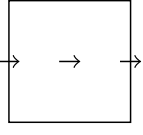
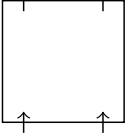
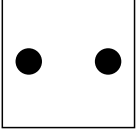
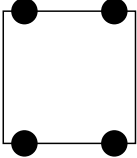
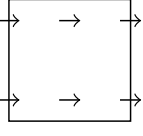
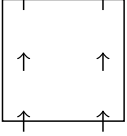
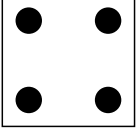
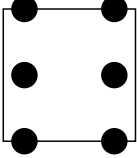
Case	\mathbb{V}_1	\mathbb{V}_2	\mathbb{V}_b	
(0, 0)	$CG_1 \otimes DG_0 + DG_0 \otimes CG_1$ 	$DG_0 \otimes DG_0$ 	$DG_0 \otimes CG_1$ 	$DG_0 \otimes CG_1$ 
(0, 1)	$CG_1 \otimes DG_1 + DG_0 \otimes CG_2$ 	$DG_0 \otimes DG_1$ 	$DG_0 \otimes DG_1$ 	$DG_0 \otimes CG_2$ 
(1, 0)	$CG_2 \otimes DG_0 + DG_1 \otimes CG_1$ 	$DG_1 \otimes DG_0$ 	$DG_1 \otimes DG_0$ 	$DG_1 \otimes CG_1$ 
(1, 1)	$CG_2 \otimes DG_1 + DG_1 \otimes CG_2$ 	$DG_1 \otimes DG_1$ 	$DG_1 \otimes DG_1$ 	$DG_1 \otimes CG_2$ 

Table 1: Function spaces constructed for each case. A filled circle on a cell edge indicates continuity across cell boundaries, while an arrow indicates the continuity of normal components of a vector across a boundary (but not continuity for the tangential components)

components and integrated the pressure gradient term by parts with the boundary terms vanishing due to the continuity of $\boldsymbol{\psi} \cdot \mathbf{n}$. $\mathbb{V}_x^{h,v}$ and $\mathbb{V}_z^{h,v}$ are the components of equation (3b) such that $\mathbb{V}_1^{h,v} = \mathbb{V}_x^{h,v} + \mathbb{V}_z^{h,v}$ with

$$\chi \in \mathbb{V}_x^{h,v} = CG_{h+1}^{0,x} \otimes DG_v^{0,z}, \quad (5)$$

$$\nu \in \mathbb{V}_z^{h,v} = DG_h^{0,x} \otimes CG_{v+1}^{0,z}, \quad (6)$$

We now calculate a discrete dispersion relation to validate the wave propagation properties of each discretisation.

5 Discrete dispersion analysis

A dispersion relation relates the frequency and wavenumber of waves. In the discrete setting, the numerical scheme determines this relation. Accurate discrete dispersion relations ensure that wave phenomena, such as inertial, gravity, and Rossby waves, are well-represented. Poor representation of such waves may result in incorrect wave speeds or computational modes. We will focus on vertical-slice test cases in which rotational forces are absent. Hence, we will not consider Rossby waves.

5.1 Analytic dispersion relation

We recall the analytical dispersion relation of the linearised compressible Boussinesq equations as a reference for the discrete analysis carried out in the later section. Seeking wavelike solutions of the form

$$(u, w, p, b) = (U, W, P, B) \exp [i(kx + lz - \omega t)]. \quad (7)$$

The linear compressible Boussinesq equations give the matrix vector system,

$$\begin{pmatrix} -i\omega & 0 & -ik & 0 \\ 0 & -i\omega & -il & -1 \\ ikc_s^2 & ilc_s^2 & -i\omega & 0 \\ 0 & N^2 & 0 & -i\omega \end{pmatrix} \begin{pmatrix} U \\ W \\ P \\ B \end{pmatrix} = 0. \quad (8)$$

The system admits a unique solution only when the determinant of the matrix vanishes. Hence,

$$\omega^4 - \omega^2[(k^2 + l^2)c_s^2 + N^2] + k^2 N^2 c_s^2 = 0, \quad (9)$$

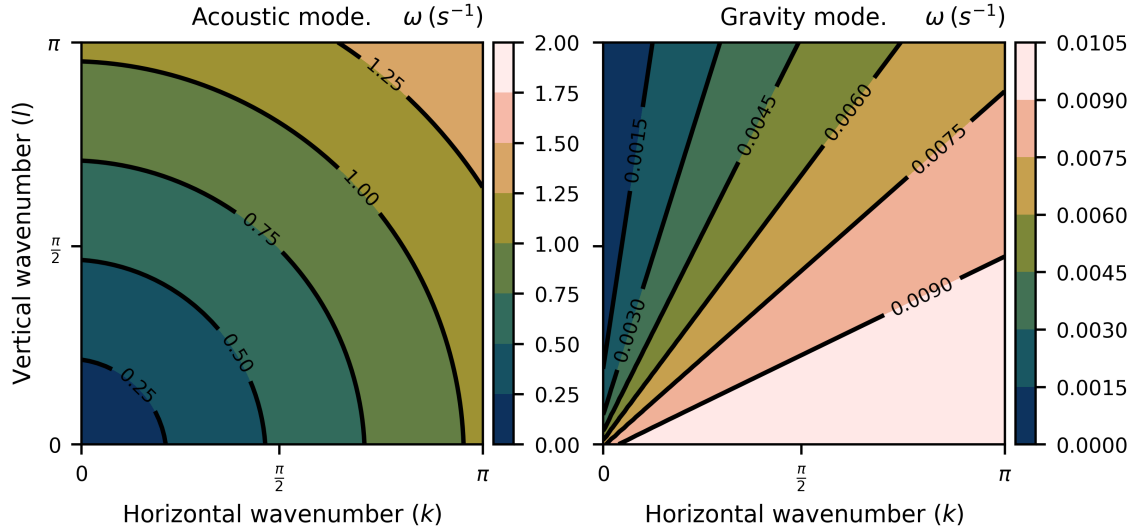


Figure 2: Analytical dispersion relation for the acoustic (left) and gravity (right) modes of the linear compressible Boussinesq equations.

which is a biquadratic equation for ω , with solutions

$$\omega^2 = \frac{1}{2}[N^2 + (k^2 + l^2)c_s^2] \left\{ 1 \pm \sqrt{1 - \frac{4k^2N^2c_s^2}{N^2 + (k^2 + l^2)c_s^2}} \right\}. \quad (10)$$

The solution with a positive sign ω_+ corresponds to acoustic waves, whilst the solution with a negative sign ω_- corresponds to gravity waves (Durrant, 2010). Assuming $N^2 \ll k^2c_s^2$, which is valid for most atmospheric applications, we simplify the equation to yield the two modes

$$\omega_+^2 \approx N^2 + (k^2 + l^2)c_s^2, \quad \omega_-^2 \approx \frac{k^2N^2}{\frac{N^2}{c_s^2} + k^2 + l^2}. \quad (11)$$

These are shown in figure 2. The frequency ω is purely real, so all modes are neutrally stable and neither grow nor decay over time. Moreover, the dispersion relations are monotonic and non-zero for all $(k, l) > 0$. We now investigate the discrete dispersion relation and demonstrate that these features persist.

5.2 Discrete dispersion relation

Recall the discretisation of the linearised compressible Boussinesq equations (4a - 4d). To construct the function spaces defined in table 1, we define a set of one-dimensional quadratic E , linear F , and

constant G basis functions across an interval $s \in [s^m, s^{m+1}]$,

$$G^{m+1/2}(s) = 1, \quad (12a)$$

$$F^m(s) = \frac{s^{m+1} - s}{s^{m+1} - s^m}, \quad (12b)$$

$$F^{m+1}(s) = \frac{s - s^m}{s^{m+1} - s^m}, \quad (12c)$$

$$E^m(s) = \left(\frac{s - s^{m+1/2}}{s^m - s^{m+1/2}} \right) \left(\frac{s - s^{m+1}}{s^m - s^{m+1}} \right), \quad (12d)$$

$$E^{m+1/2}(s) = \left(\frac{s - s^m}{s^{m+1/2} - s^m} \right) \left(\frac{s - s^{m+1}}{s^{m+1/2} - s^{m+1}} \right), \quad (12e)$$

$$E^{m+1}(s) = \left(\frac{s - s^m}{s^{m+1} - s^m} \right) \left(\frac{s - s^{m+1/2}}{s^{m+1} - s^{m+1/2}} \right). \quad (12f)$$

Taking tensor products of these one-dimensional basis functions defines the two-dimensional basis functions. We now define the derivation of the dispersion relation for the $(1, 0)$ case. The other cases follow similarly. In the $(1, 0)$ case, the basis functions are linear and quadratic for the horizontal direction and linear and constant for the vertical direction

$$\chi_{1,2,3} = \{E^m(x)G^{n+1/2}(z), E^{m+1/2}(x)G^{n+1/2}(z), E^{m+1}(x)G^{n+1/2}(z)\}, \quad (13a)$$

$$(\nu, \gamma)_{1,2,3,4} = \{F^m(x)F^n(z), F^{m+1}(x)F^n(z), F^m(x)F^{n+1}(z), F^{m+1}(x)F^{n+1}(z)\}, \quad (13b)$$

$$\psi_{1,2} = \{F^m(x)G^{n+1/2}(z), F^{m+1}(x)G^{n+1/2}(z)\}. \quad (13c)$$

The prognostic variables restricted to a single element $[x^m, x^{m+1}] \times [z^m, z^{m+1}]$ are

$$\hat{u}(x, z) = u_{(0,+)}^{m,n+1/2} \chi_1 + u_{(+,+)}^{m+1/2,n+1/2} \chi_2 + u_{(0,+)}^{m+1,n+1/2} \chi_3, \quad (14a)$$

$$\hat{w}(x, z) = v_{(+,0)}^{m,n} \nu_1 + v_{(+,0)}^{m+1,n} \nu_2 + v_{(-,0)}^{m,n+1} \nu_3 + v_{(-,0)}^{m+1,n+1} \nu_4, \quad (14b)$$

$$\hat{p}(x, z) = p_{(+,+)}^{m,n+1/2} \psi_1 + p_{(-,+)}^{m+1,n+1/2} \psi_2 \quad (14c)$$

$$\hat{b}(x, z) = b_{(+,0)}^{m,n} \gamma_1 + b_{(+,0)}^{m+1,n} \gamma_2 + b_{(-,0)}^{m,n+1} \gamma_3 + b_{(-,0)}^{m+1,n+1} \gamma_4, \quad (14d)$$

where the subscripts $(0, -, +)$ denote whether the field is continuous (0) or discontinuous $(+, -)$ at this DoF, the $(+, -)$ denotes which side of the facet the discontinuous DoF belongs. It is helpful to

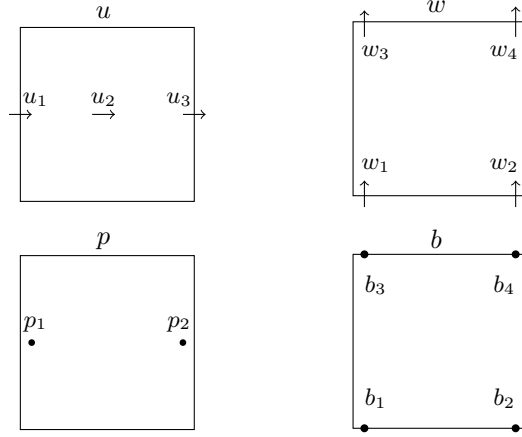


Figure 3: Locations of degrees of freedom for the (1,0) case for the horizontal velocity field (u) shown in the top left, followed by the vertical velocity field (w) in the top right, the pressure field (p) in the bottom left, and the buoyancy field (b) in the bottom right. The node numbering can be related to node locations using equations (15). Nodes on a cell edge indicate continuity between cells, and an arrow across an edge indicates normal continuity.

number the DoFs for each cell such that,

$$(u_1, u_2, u_3) = (u^{m,n+1/2}, u^{m+1/2,n+1/2}, u^{m+1,n+1/2}), \quad (15a)$$

$$(w_1, w_2, w_3, w_4) = (w^{m,n}, w^{m+1,n}, w^{m,n+1}, w^{m+1,n+1}), \quad (15b)$$

$$(p_1, p_2) = (p^{m,n+1/2}, p^{m+1,n+1/2}), \quad (15c)$$

$$(b_1, b_2, b_3, b_4) = (b^{m,n}, b^{m+1,n}, b^{m,n+1}, b^{m+1,n+1}). \quad (15d)$$

Figure 3 shows the locations of these nodes (node locations of the (0, 1) can be found in appendix A). Substituting the variable expansions (14a - 14d) into the discretised equations (4a - 4d), gives an equation for each distinct DoF. For example, consider solving equation (4a) on a generic cell $(x, z) \in [x^m, x^{m+1}] \times [z^n, z^{n+1}]$, this yields the system of equations

$$\int_{x^m}^{x^{m+1}} \int_{z^n}^{z^{n+1}} \frac{\partial \hat{u}}{\partial t} \chi_1 dx dz + \int_{x^m}^{x^{m+1}} \int_{z^n}^{z^{n+1}} \hat{p} \frac{\partial \chi_1}{\partial x} dx dz = 0, \quad (16a)$$

$$\int_{x^m}^{x^{m+1}} \int_{z^n}^{z^{n+1}} \frac{\partial \hat{u}}{\partial t} \chi_2 dx dz + \int_{x^m}^{x^{m+1}} \int_{z^n}^{z^{n+1}} \hat{p} \frac{\partial \chi_2}{\partial x} dx dz = 0, \quad (16b)$$

$$\int_{x^m}^{x^{m+1}} \int_{z^n}^{z^{n+1}} \frac{\partial \hat{u}}{\partial t} \chi_3 dx dz + \int_{x^m}^{x^{m+1}} \int_{z^n}^{z^{n+1}} \hat{p} \frac{\partial \chi_3}{\partial x} dx dz = 0. \quad (16c)$$

As in the analytical case, we assume that all variables are wavelike,

$$(u, w, p, b)^{m,n} \equiv (U, W, P, B) \exp[i(kx^m + lz^n - \omega t)], \quad (17)$$

where the (m, n) superscripts define the location of the DoF as in (15). Exploiting the wave structure, we reduce the three-equation system (16) to two equations. The continuity of the field at the DoF allows us to relate the field values at the left and right edge DoFs, leaving only two unique DoFs per cell. Explicitly, this is done by first relating the DoF u_3 to u_1 via,

$$u_3 = u_1 e^{ik\Delta x}, \quad (18)$$

such that,

$$\hat{u}(x, z) = u_1 \chi_1 + u_2 \chi_2 + u_1 e^{ik\Delta x} \chi_3. \quad (19)$$

Having related u_3 to u_1 , we next relate their corresponding equations. Each m is replaced by $m - 1$ in equation (14a), this results in a ‘shifting’ of the equation by a factor of $e^{-ik\Delta x}$ to yield,

$$\hat{u}_{right} = u_1 \chi_1 e^{(-ik\Delta x)} + u_2 \chi_2 e^{(-ik\Delta x)} + u_1 \chi_3. \quad (20)$$

We then add this ‘shifted’ u_3 equation to the equation for u_1 to get an expansion centred on u_1 ,

$$\begin{aligned} \hat{u}_{center} &= \hat{u} + \hat{u}_{right} \\ &= u_1 \chi_1 e^{(-ik\Delta x)} + u_2 \chi_2 e^{(-ik\Delta x)} + u_1 (\chi_3 + \chi_1) + u_2 \chi_2 + u_1 \chi_3 e^{ik\Delta x}. \end{aligned} \quad (21)$$

We repeat this process for the pressure expansion equation (14c). Unlike the horizontal velocity expansion, there is no continuity to relate nodes to each other, hence

$$\begin{aligned} \hat{p}_{center} &= \hat{p} + \hat{p}_{right} \\ &= p_1 \psi_1 e^{(-ik\Delta x)} + p_2 \psi_2 e^{(-ik\Delta x)} + p_1 \psi_1 + p_2 \psi_2. \end{aligned} \quad (22)$$

The system of equations in (16) has been reduced to a set of two equations,

$$\int_{x^m}^{x^{m+1}} \int_{z^n}^{z^{n+1}} \frac{\partial \hat{u}_{center}}{\partial t} \chi_1 dx dz + \int_{x^m}^{x^{m+1}} \int_{z^n}^{z^{n+1}} \hat{p}_{center} \frac{\partial \chi_1}{\partial x} dx dz = 0, \quad (23a)$$

$$\int_{x^m}^{x^{m+1}} \int_{z^n}^{z^{n+1}} \frac{\partial \hat{u}}{\partial t} \chi_2 dx dz + \int_{x^m}^{x^{m+1}} \int_{z^n}^{z^{n+1}} \hat{p} \frac{\partial \chi_2}{\partial x} dx dz = 0. \quad (23b)$$

The same logic can be applied to the vertical velocity and buoyancy equations, as they are continuous in the vertical direction. We follow the same procedure of first relating $(w, b)_3$ to $(w, b)_1$ and $(w, b)_4$

to $(w, b)_2$ via,

$$\begin{aligned}(w_3, b_3) &= (w_1, b_1)e^{il\Delta z}, \\ (w_4, b_4) &= (w_2, b_2)e^{il\Delta z}.\end{aligned}$$

Next, we replace each n with $n - 1$ in equations (14b) and (14d) for the equations at nodes $(w, b)_{3,4}$ to ‘shift’ each equation by a factor of $e^{il\Delta z}$, and then add them to the corresponding equations for $(w, b)_{1,2}$. This procedure yields a system of eight equations, two for each variable. Writing this in matrix form yields the system

$$\begin{pmatrix} -i\omega\mathbf{M}_u & 0 & \mathbf{D}_x^u & 0 \\ 0 & -i\omega\mathbf{M}_w & \mathbf{D}_z^w & -\mathbf{Q} \\ c_s^2\mathbf{D}_x^p & c_s^2\mathbf{D}_z^p & -i\omega\mathbf{M}_p & 0 \\ 0 & N^2\mathbf{Q}^T & 0 & -i\omega\mathbf{M}_b \end{pmatrix} \begin{pmatrix} \bar{\mathbf{U}} \\ \bar{\mathbf{W}} \\ \bar{\mathbf{P}} \\ \bar{\mathbf{B}} \end{pmatrix} = 0, \quad (24)$$

where $(\bar{\mathbf{U}}, \bar{\mathbf{W}}, \bar{\mathbf{P}}, \bar{\mathbf{B}})$, are vectors of the amplitude factors for the basis functions of each prognostic variable such as $\bar{\mathbf{U}} = (U_1, U_2)^T$ etc. $M_{u,w,p,b}$, $D_{x,z}^{u,w,p}$ and Q are all 2×2 matrices that represent the action of mass matrices, discrete derivative matrices, and projection matrices, respectively (details of these matrices can be found in appendix B). Splitting equation (24) into its symmetric and non-symmetric components yields

$$-i\omega\mathcal{M}\hat{\mathbf{x}} + \mathcal{S}\hat{\mathbf{x}} = 0, \quad (25)$$

where

$$\mathcal{M} = \begin{pmatrix} \mathbf{M}_u & 0 & 0 & 0 \\ 0 & \mathbf{M}_w & 0 & 0 \\ 0 & 0 & \mathbf{M}_p & 0 \\ 0 & 0 & 0 & \mathbf{M}_b \end{pmatrix}, \quad (26)$$

$$\mathcal{S} = \begin{pmatrix} 0 & 0 & \mathbf{D}_x^u & 0 \\ 0 & 0 & \mathbf{D}_z^w & \mathbf{Q} \\ \mathbf{D}_x^p & \mathbf{D}_x^p & 0 & 0 \\ 0 & \mathbf{Q}^T & 0 & 0 \end{pmatrix}, \quad (27)$$

and $\hat{\mathbf{x}} = [U_1, U_2, W_1, W_2, P_1, P_2, B_1, B_2]^T$. As \mathcal{M} is a block diagonal matrix of mass matrices, we know that its inverse exists such that equation (25) can be rearranged to give,

$$\omega \hat{\mathbf{x}} = -i\mathcal{M}^{-1}\mathcal{S}\hat{\mathbf{x}} = \mathcal{F}\hat{\mathbf{x}}. \quad (28)$$

We have now formed an eigenvalue problem which, for a given wavenumber pair (k, l) , can be solved to yield eigenvalues ω corresponding to the linear acoustic and gravity modes.

5.2.1 Wave mode allocation

As the matrix \mathcal{F} has dimensions 8×8 , we extract eight eigenvalue solutions from equation (28). These solutions correspond to the sets,

$$\pm\{\omega_1^+, \omega_2^+\} \quad \pm\{\omega_1^-, \omega_2^-\}, \quad (29)$$

where ω^+ represents the acoustic waves and ω^- the gravity waves. Taking the positive values of these sets, we now have two solutions for each regime instead of the single solution in the analytical case. As in (Melvin *et al.*, 2018, 2014) we argue that this extra solution corresponds to an aliased wave from a higher wavenumber, supported by the increased finite element order in the horizontal direction. Specifically, we say one solution belongs to the initial wavenumber space $(k\Delta x, l\Delta z) \in (0, \pi) \times (0, \pi)$ and the other solution corresponds to an x -extended wavenumber space $(k\Delta x, l\Delta z) \in (\pi, 2\pi) \times (0, \pi)$. We must now determine which solutions belong to which space. To do this, we split the wavenumber space into sectors corresponding to the wavenumber extension and compute all possible permutations of ω for each sector. We measure the error between the discrete and analytic dispersion relations for each permutation of ω , using the L_2 norm, and choose the permutation with the lowest error. To calculate the dispersion relation for the $(0, 1)$ and $(1, 1)$ cases we follow the same procedure as the $(1, 0)$ case, with the $(0, 1)$ case being extended in the z direction and $(1, 1)$ in both directions.

We examine how closely our discrete dispersion relations match the analytical dispersion relation plotted in figure 2. Figure 4 shows the discrete dispersion relation for each of the four cases. To allow for comparison to the analytical dispersion relation, we use scaled wavenumbers

$$(\tilde{k}, \tilde{l}) \in \left[0, \frac{2\pi}{\Delta x}\right] \times \left[0, \frac{2\pi}{\Delta z}\right], \quad (30)$$

In general, all cases provide a good representation of the analytical dispersion relation, with a few noted inaccuracies. Each case overestimates the acoustic mode as (\tilde{k}, \tilde{l}) approaches $(\frac{2\pi}{\Delta x}, \frac{2\pi}{\Delta z})$, whilst the

Dispersion relation errors for different configurations

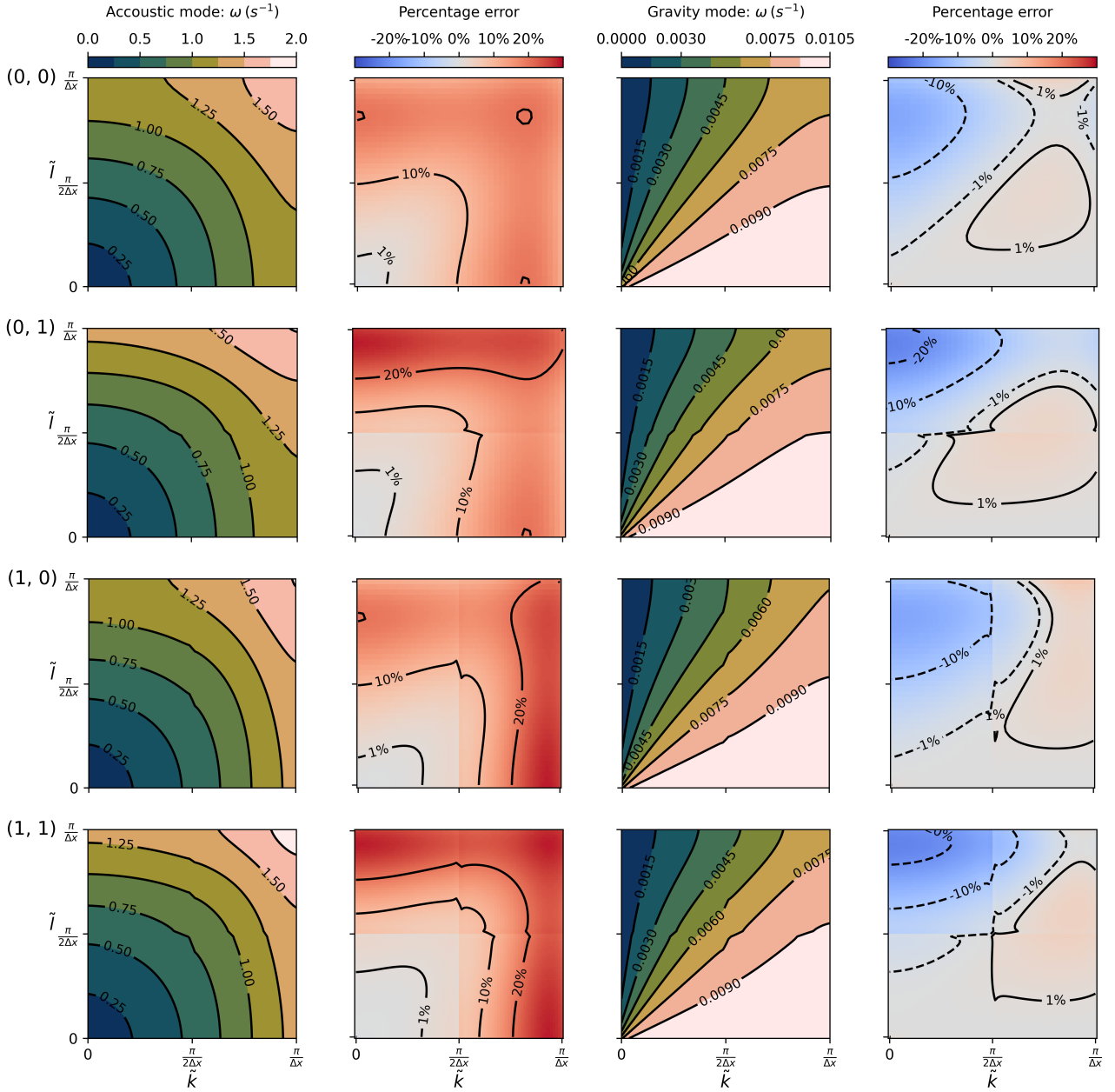


Figure 4: Discrete dispersion relations for the (1, 1), (1, 0) and (0, 1) finite element cases, for the scaled wavenumbers $\tilde{k}, \tilde{l} \in [0, \frac{2\pi}{\Delta x}] \times [0, \frac{2\pi}{\Delta z}]$, where we arbitrarily take $(\Delta x, \Delta z) = (1000, 1000)$ m. To the right of each mode is a plot showing the percentage error between the discrete and analytical dispersion relations.

Case	Normalised L_2 error norm (10^{-4})	Max error	Min error
(0, 0)	1.42719	0.0278812	1.89524e-10
(0, 1)	1.63875	0.0496205	1.30731e-10
(1, 0)	1.2243	0.0279968	2.92222e-11
(1, 1)	1.36044	0.0497644	3.9529e-12

Table 2: Global error measured for the gravity mode. Increasing horizontal order improves the representation of the gravity mode; however, increasing the vertical order degrades it. We do, however, generally see a larger maximum error with increasing order.

gravity mode is underestimated for waves with high \tilde{l} but low \tilde{k} . Although we have derived the discrete dispersion relations for gravity and acoustic waves, we now focus solely on gravity waves, as acoustic waves are not important for weather and climate modelling and are typically damped or filtered by numerical schemes. When comparing different orders, we find that increasing order in either direction introduces spectral gaps in the dispersion relation along the lines $\tilde{k} = \pi/\Delta x$ and $\tilde{l} = \pi/\Delta z$, in addition higher order cases represent larger wavenumbers less accurately however improve the representation of wavenumbers $\tilde{k}, \tilde{l} < \frac{\pi}{2\Delta x}$. Table 2 shows some error statistics for the gravity mode (acoustic mode statistics can be found in appendix C). These statistics, combined with the results presented in figure 4 indicate that the vertical order is the largest contributor to overall error. The (0,1) case has the most significant maximum error and performs worse than (0,0) in the L_2 norm. In contrast, increasing the horizontal order, such as in (1,0) improves the L_2 norm error with only a marginal cost to the most extreme errors. The order (1,1) case has a worse performance when compared to the (1,0) case, but is still better than the (0,1) and (0,0) cases for the global norm, however, does possess a maximal error comparable to the (0,1) case. Having identified some potential shortcomings from the dispersion relation, specifically, the propagation of near grid-scale waves, we now wish to see if these issues materialise in the numerical model.

6 Model formulation

Our model is implemented in Gusto, the dynamical core toolkit built on the Firedrake finite element library. Firedrake provides an automatic code generation for the implementation of finite element methods to solve partial differential equations (Ham *et al.*, 2023). Gusto provides a suite of stable time stepping, transport and physics schemes for discretising and modelling both the shallow water equations and the compressible Euler equations, facilitating rapid prototyping of novel algorithms within the compatible finite element framework.

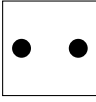
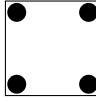
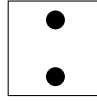
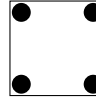
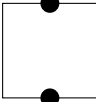
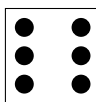
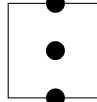
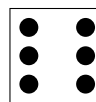
Variable	Case (1, 0)		Case (0, 1)	
	V_0	V_E	V_0	V_E
ρ				
u				
w				
b or θ				

Table 3: A table illustrating the initial and embedded spaces used in the (1, 0) and (0, 1) cases, here u and w indicate the horizontal and vertical components of the velocity vector \mathbf{u} . Nodes indicate the location of DoFs within the space, with nodes placed on a cell edge indicating continuity, arrows indicate a vector value DoF and arrows across a cell edge indicate normal continuity across that edge.

6.1 Time discretisation

In all test cases, the prognostic variables are evolved in time using a semi-implicit quasi-Newton time-stepping scheme. The next-generation UK Met Office model influenced this choice; a detailed description of the scheme is found in (Wood *et al.*, 2014; Melvin *et al.*, 2019; Bendall *et al.*, 2019; Hartney *et al.*, 2025). Within the semi-implicit quasi-Newton scheme, we apply an explicit transport scheme to each of the prognostic variables. In this paper, we use the SSPRK3 scheme for all variables (Izzo and Jackiewicz, 2022) and pseudo code outlining the timestepping procedure can be found in appendix D.

Second-order transport is a minimum requirement for accurate weather and climate models (Stanforth and Thuburn, 2012). For the (1, 1) case, we employ an upwind scheme to evaluate the transport terms. However, when the model configuration includes lowest-order finite elements, we cannot achieve second-order accuracy through upwinding alone. To overcome this, we make use of the recovered space finite element transport scheme from (Bendall *et al.*, 2019; Bendall and Wimmer, 2023).

The recovered space transport scheme achieves second-order transport by computing the transport step in a higher-order space (the embedding space) before projecting the transported field back to the original space. As long as the projection operator is second-order accurate, the entire scheme is second-order accurate. For the (0, 0) case (Bendall and Wimmer, 2023) describes a sequence of operators and space that satisfy second order accuracy; however, we now must extend this to the (1, 0) and (0, 1) cases by defining the respective embedding spaces.

Table 3 shows the initial space V_0 of each variable and the embedding V_E space in which the

transport occurs. The field is reconstructed in the embedding space via a continuous version of the higher order space using recovery operators described in (Bendall and Wimmer, 2023). This method replaces the DG upwind method whenever a lowest-order polynomial is present.

7 Numerical tests

We now explore the accuracy and convergence properties of the split-order schemes over a suite of numerical test cases. When comparing numerical results from different order schemes, we keep the distance between DoFs constant by adjusting the cell size to account for the additional DoFs in the higher-order representation. Details of the resolutions used can be found in appendix E). Throughout this section, the model setup will be described in the context of the (1, 1) case unless otherwise stated.

7.1 Skamarock and Klemp gravity wave

To support the theoretical findings of the discrete dispersion analysis, we consider a wave propagation benchmark of the non-hydrostatic gravity wave of (Skamarock and Klemp, 1994). This test examines the horizontal propagation of gravity waves in a two-dimensional Cartesian vertical slice domain $[0, L] \times [0, H]$ km. We initialise the test with a balanced, thermally stratified base state and introduce a buoyancy perturbation

$$b' = b_0 \sin\left(\frac{\pi z}{H}\right) \left[1 + \frac{x - x_c}{a^2}\right]. \quad (31)$$

Where $b_0 = 0.001 \text{ m s}^{-2}$, $H = 10 \text{ km}$, $a = 5 \text{ km}$ and centred on $x_c = \frac{L}{2} \text{ km}$ where $L = 300 \text{ km}$. This perturbation triggers a gravity wave that propagates along the domain. The integration is carried out for $t = 3600 \text{ s}$ in time steps of $\Delta t = 1.2 \text{ s}$. For the order (1, 1) case the resolution is $(\Delta x, \Delta z) = (2000 \text{ m}, 2000 \text{ m})$ and the other cases have suitably scaled resolutions to ensure that each case has the same total number of DoFs and has the same effective resolution. Figure 5 shows the final buoyancy field, and we see that all cases show correct wave propagation. We also carry out a convergence test: we compute the L_2 error norm by comparing simulation with $\Delta x \in [450, 500, 600, 700, 750, 800, 850, 900] \text{ m}$ against a high-resolution reference solution computed with $\Delta x = 120 \text{ m}$, which we treat as the truth. We keep vertical resolution $\Delta z = 1000 \text{ m}$, and time step $\Delta t = 1.2 \text{ s}$ constant for all simulations. The results presented in figure 6 demonstrate an order of convergence of at least two for all cases, and the (1, 0) and (1, 0) cases have a convergence rate approaching third order, the largest order permitted by our time-stepping and transport schemes.

These results suggest that the horizontal order is dominating the accuracy for this test case. This result is expected, since the gravity wave test case consists of predominantly horizontal motion, exten-

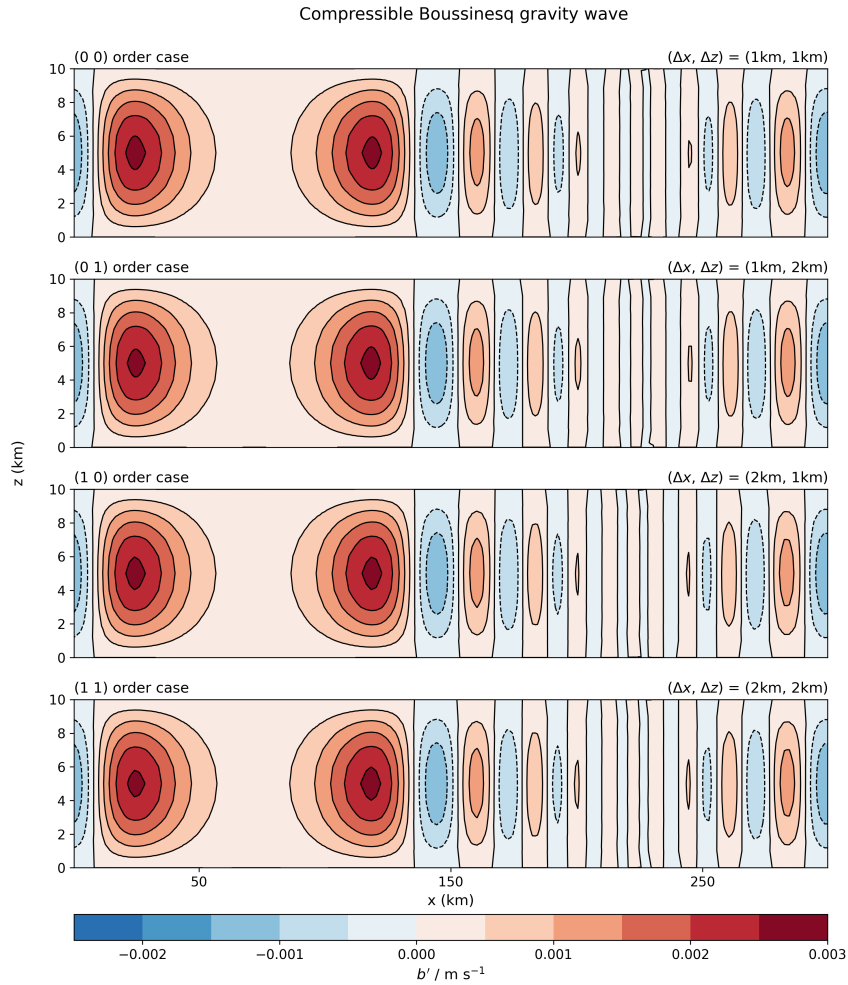


Figure 5: Buoyancy perturbation of the Skamarock and Klemp gravity wave for the compressible boussinesq equations, test case at time $t=3600s$. Contours are between $[-3, 3] \times 10^{-3} \text{ m s}^{-2}$ with a spacing of $0.5 \times 10^{-3} \text{ m s}^{-2}$ and are the same for each case.

Convergence plot for the b field

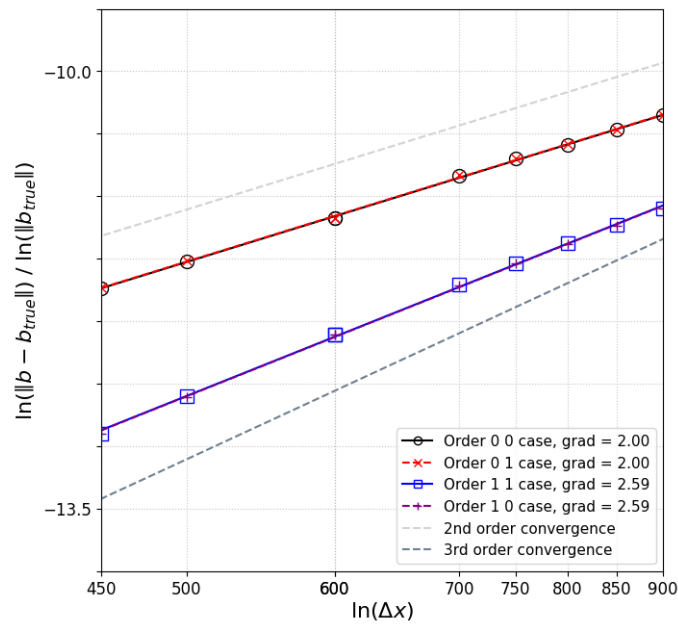


Figure 6: Convergence plot of the buoyancy field. Two comparison lines are also shown, to demonstrate second and third order convergence.

sive testing has found that vertical resolution generally plays little role in the convergence or accuracy of the solution.

7.2 Travelling Vortex

The travelling vortex test case first proposed in (Kadioglu *et al.*, 2008), formulated in line with (Chew *et al.*, 2021; Kowalczyk, 2025), consists of a smooth vortex in a doubly periodic two-dimensional domain of dimensions $[0, 10] \times [0, 10]$ km with no Coriolis or gravitational forces. We initialise the vortex with a smooth radially symmetric density bump placed at the domain's centre (5, 5)km.

We are interested in how each order case represents scenarios in which horizontal or vertical motion dominate. Accordingly, we prescribe three advecting velocities: a purely horizontal flow $\mathbf{u} = (100, 0)\text{m s}^{-1}$, a purely vertical flow $\mathbf{u} = (0, 100)\text{m s}^{-1}$, and a diagonal flow $\mathbf{u} = (100, 100)\text{m s}^{-1}$.

We run each simulation to $t = 100\text{s}$ with a time step of $\Delta t = 0.1\text{s}$, ensuring that the vortex undergoes one complete traversal of the domain. The spatial resolution of the (1, 1) case is (200, 200)m and other cases are scaled appropriately. For each case, we compute the L_2 error between the initial and final density fields and plot it as a function of the overall cell size. Figure 7 demonstrates a clear relationship between convergence behaviour and the dominant direction of motion. For horizontal advection, the (1, 1) and (1, 0) cases converge more rapidly than the (0, 0) and (0, 1) cases. Conversely, under vertical advection, the vertical order governs convergence, with the corresponding pair performing better. When the vortex is advected diagonally across the domain, the (0, 0), (1, 0), and (0, 1) cases exhibit the same convergence rate but differ in their absolute error levels, while the (1, 1) case achieves both a lower error and a higher convergence rate. Increasing the order, therefore, systematically improves the convergence properties of the scheme for motion aligned with that direction.

7.3 Schär Mountain wave

So far, we have focused on the convergence order of the split-order scheme; however, accuracy considerations are equally important. As discussed in section 5, increasing the polynomial order improves the representation of low wavenumbers, but introduces spectral gaps and degrades the representation of high wavenumbers. To assess these competing effects, we consider the test case of Schär *et al.* (Schär *et al.*, 2002), which excites a broad range of wavenumbers. We initialise a balanced atmosphere over a mountain range expressed by,

$$h(x) = h_0 \exp\left(-\left(\frac{x}{a}\right)^2\right) \cos^2\left(\frac{\pi x}{\lambda}\right), \quad (32)$$

Convergence plots for the ρ field

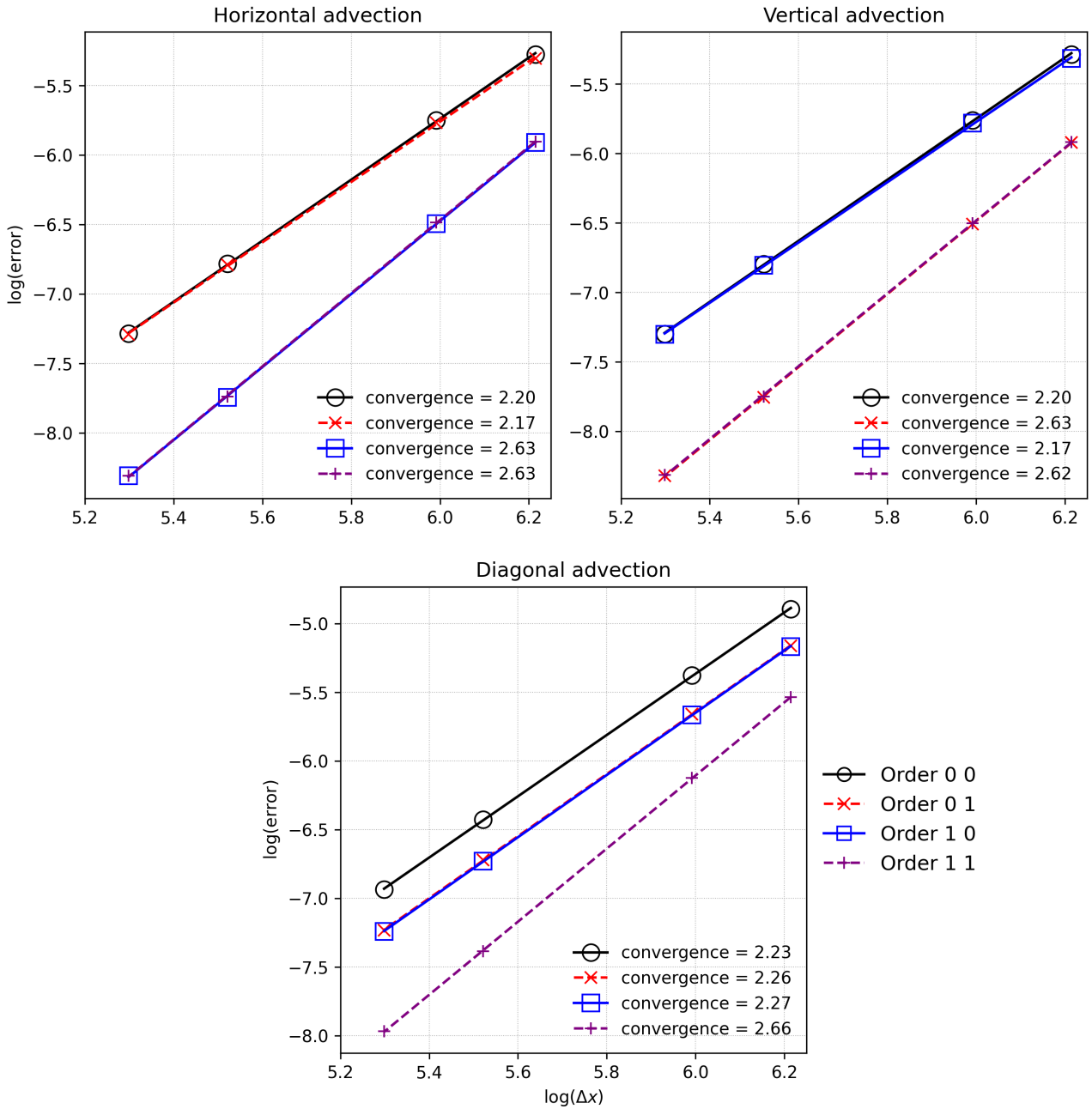


Figure 7: Convergence plots for each of the advection cases. Going left to right the advecting velocities are, $((100\text{ms}^{-1}, 0))$ for the horizontal, $(0, 100\text{ms}^{-1})$ for the vertical and, $(100\text{ms}^{-1}, 100\text{ms}^{-1})$ for the diagonal.

Schär Mountain wave for different order cases

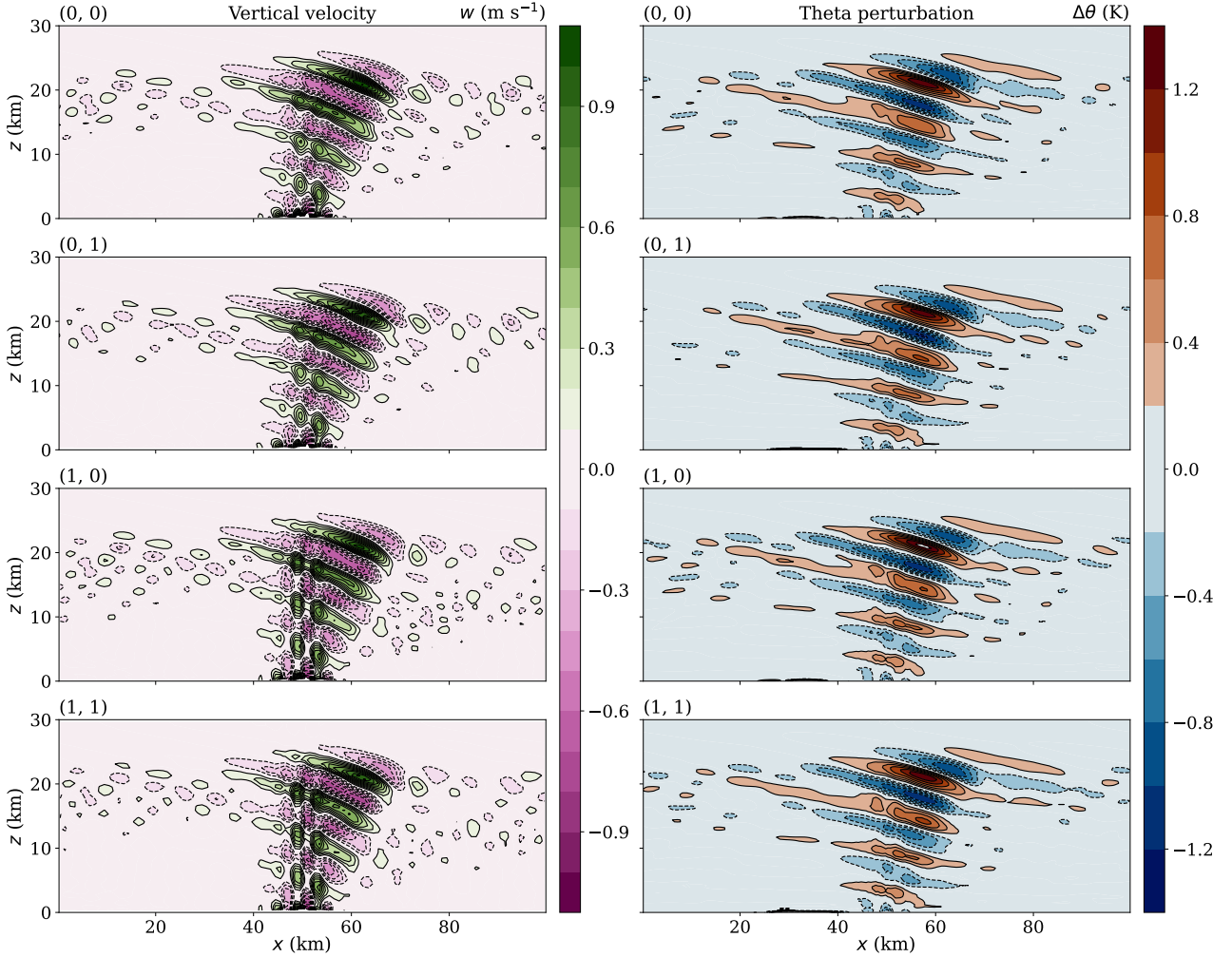


Figure 8: Plots of the vertical velocity (left) and theta perturbation (right) for the Schär mountain wave test case at $t = 3600s$. Resolution for the four cases are, order (1, 1): (1000, 600)m, order (1, 0): (1000, 300)m, order (0, 1): (500, 600)m and order (0, 0): (500, 300)m.

where $h_0 = 250$ m, $a = 5 \times 10^3$ m, and $\lambda = 4 \times 10^3$ m. We calculate the simulation in a domain of dimensions $[-L/2, L/2] \times [0, 30]$ km where $L = 100$ km. The velocity is initially horizontal with $u = 10$ m s $^{-1}$ and the potential temperature field has a profile of

$$\theta_b = T_{surf} \exp\left(-\frac{N^2 z}{g}\right), \quad T_{surf} = 288 \text{ K}, \quad (33)$$

where $N = 0.01$ s $^{-1}$ and $g = 9.810616$ m s $^{-2}$. The atmosphere is initialised in hydrostatic balance following the procedure described in (Cotter and Shipton, 2022). In addition, we need to adjust the implicit-to-explicit ratio of our time-stepper by setting $\alpha = 0.51$. This adjustment makes the time scheme slightly more implicit and dampens the most extreme grid-scale waves. This choice is standard for semi-implicit quasi-Newton time schemes implemented in full NWP models Benacchio and Wood (2016). We present results of the Schär mountain wave test in figure 8. Each case provides a solution

that is consistent with those found in the literature (Giraldo and Restelli, 2008; Cotter, 2023; Schär *et al.*, 2002). Whilst the theta perturbation is largely identical across the cases, for the vertical velocity, we can see that the higher horizontal cases (1, 1) and (1, 0) contain more pronounced vertical velocity packets at 10 km and to the right of the mountain peak.

7.4 Baroclinic Wave

Finally, we demonstrate the successful implementation of the split-order schemes on an Earth-sized domain with a deep atmosphere using the dry baroclinic wave described in Ullrich *et al.* (2014). We initialise the test on a cubed sphere grid with appropriate resolutions (see appendix E). Each simulation was run for 10 days, with a time step of $\Delta t = 450.0$ s for all cases. Plots of the surface pressure and temperature at days 8 and ten 10 can be seen in figures 9 and 10.

Each case produces a solution that agrees with the results present in the literature (Ullrich *et al.*, 2014; Wood *et al.*, 2014; Melvin *et al.*, 2024; Giraldo *et al.*, 2024; Skamarock *et al.*, 2021) and the solutions exhibit pressure perturbations at the same locations.

8 Conclusion

The paper has focused on demonstrating the split-order scheme’s accuracy and flexibility; however, the computational impacts of independently varying the horizontal and vertical polynomial orders remain to be fully characterised. Through a discrete dispersion analysis of the compressible Boussinesq equations, we have examined how differing horizontal and vertical polynomial orders affect wave propagation. Higher-order discretisations reduce dispersion error at slow and intermediate wavenumbers but can introduce spectral gaps and increased error near the grid scale. The gravity wave mode was found to be particularly sensitive to changes in the vertical polynomial order, highlighting the importance of vertical discretisation choices in atmospheric models. To further explore these findings, a suite of numerical test cases in section 7 demonstrated that increasing the polynomial order in a given direction improves convergence in that direction, with the horizontal order having a consistently larger impact under typical atmospheric conditions. Qualitative tests showed no evidence of spurious grid-scale wave activity associated with higher-order discretisations, despite concerns suggested by the dispersion analysis. Across all configurations, the split-order schemes reproduced results reported in the existing literature, supporting the use of polynomial order as a practical means of tuning the numerical behaviour of a dynamical core. While the present study has focused primarily on accuracy considerations, it is important to note that computational efficiency and the interaction between split-order discretisations and physical parameterisations are also critical aspects of dynamical core design. Thus,

Baroclinic Wave at 8.0 days

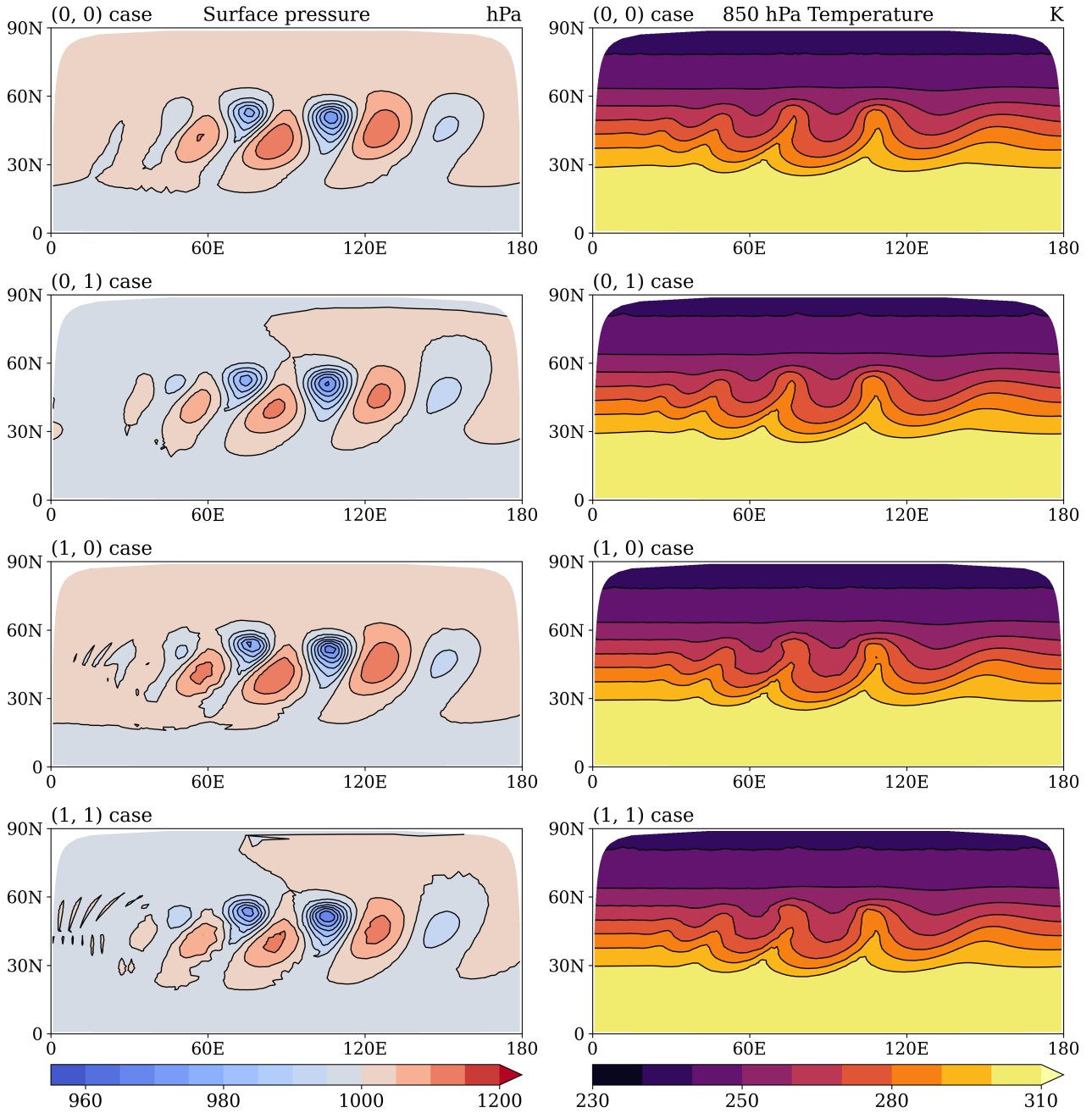


Figure 9: Plots of the surface pressure (left) and surface temperature (right) at day 8 of integration. The rows correspond to the different finite element orders.

Baroclinic Wave at 10.0 days

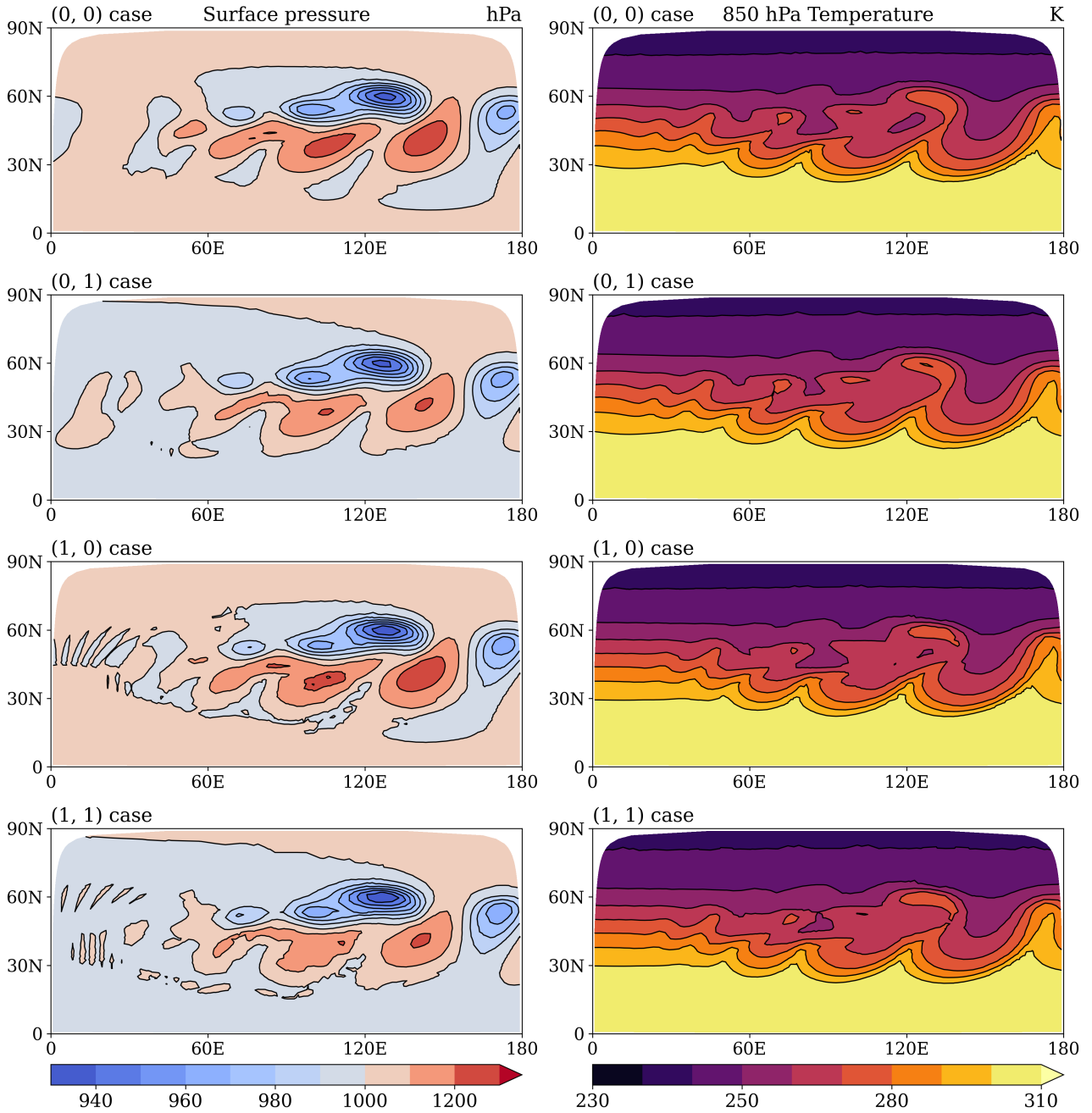


Figure 10: Plots of the surface pressure (left) and surface temperature (right) at day 10 of integration. The rows correspond to the different finite element orders.

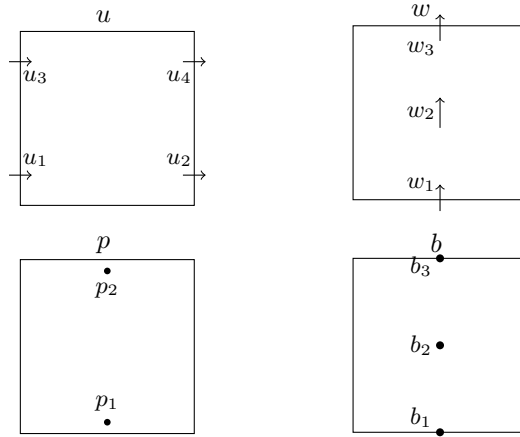


Figure 11: Locations of degrees of freedom for the (1,0) case for the horizontal velocity field (u) shown in the top left followed by the vertical velocity field (w) in the top right, pressure field (p) in the bottom left and the buoyancy field (b) in the bottom right. The node numbering can be related to node location by using equation (15)

the implications of split polynomial order for performance and physics–dynamics coupling remain open questions and represent important directions for future work.

Acknowledgements

This research was funded by the Faculty of Environment Science and Economy at the University of Exeter. The authors would also like to thank Karina Kowalczyk for help with the initialisation of the travelling vortex test case. For the purpose of open access, the authors have applied a ‘Creative Commons Attribution (CC BY) licence to any Author Accepted Manuscript version arising from this submission.

A (0, 1) node location

The DoF locations for the finite elements with horizontal order 0 and vertical order 1 are shown in figure 15.

B Dispersion matrices

Details of the mass and discrete derivative matrices for the (1,0) case can be found in section B.1 and matrices for the (0,1) case in section B.2. Details of the relevant matrices for the (1,1) and (0,0) cases can be found in Melvin *et al.* (2018).

B.1 (1, 0) Case

$$M_u = \frac{\Delta x \Delta z}{30} \begin{pmatrix} (8 - 2 \cos(k\Delta x)) e^{il\Delta z/2} & 4 \cos\left(\frac{k\Delta x}{2}\right) e^{il\Delta z/2} \\ (2 e^{ik\Delta x} + 2) e^{il\Delta z/2} & 16 e^{ik\Delta x/2} e^{il\Delta z/2} \end{pmatrix}. \quad (34)$$

$$M_w = M_b = Q = \frac{\Delta x \Delta z}{36} \begin{pmatrix} 4(\cos(l\Delta z) + 2) & 2(\cos(l\Delta z) + 2) e^{ik\Delta x} \\ 2(\cos(l\Delta z) + 2) & 4(\cos(l\Delta z) + 2) e^{ik\Delta x} \end{pmatrix}. \quad (35)$$

$$M_p = \frac{\Delta x \Delta z}{6} \begin{pmatrix} 2 e^{il\Delta z/2} & e^{il\Delta z/2} e^{ik\Delta x} \\ e^{il\Delta z/2} & 2 e^{il\Delta z/2} e^{ik\Delta x} \end{pmatrix}. \quad (36)$$

$$D_x^u = \frac{\Delta z}{6} \begin{pmatrix} (5 - e^{-ik\Delta x}) e^{il\Delta z/2} & (e^{ik\Delta x} - 5) e^{il\Delta z/2} \\ -4 e^{il\Delta z/2} & 4 e^{il\Delta z/2} e^{ik\Delta x} \end{pmatrix}. \quad (37)$$

$$D_x^p = \frac{\Delta z}{6} \begin{pmatrix} (e^{ik\Delta x} - 5) e^{il\Delta z/2} & 4 e^{il\Delta z/2} e^{ik\Delta x/2} \\ (5 e^{ik\Delta x} - 1) e^{il\Delta z/2} & -4 e^{il\Delta z/2} e^{ik\Delta x/2} \end{pmatrix}. \quad (38)$$

$$D_z^w = \frac{\Delta x}{6} \begin{pmatrix} 4 i \sin(l\Delta z/2) & 2 i \sin(l\Delta z/2) e^{ik\Delta x} \\ 2 i \sin(l\Delta z/2) & 4 i \sin(l\Delta z/2) e^{ik\Delta x} \end{pmatrix}. \quad (39)$$

$$D_z^p = \frac{\Delta x}{6} \begin{pmatrix} 2(e^{il\Delta z} - 1) & (e^{il\Delta z} - 1) e^{ik\Delta x} \\ (e^{il\Delta z} - 1) & 2(e^{il\Delta z} - 1) e^{ik\Delta x} \end{pmatrix}. \quad (40)$$

B.2 (0, 1) Case

$$M_u = \begin{pmatrix} 4(\cos(k\Delta x) + 2) & 2(\cos(k\Delta x) + 2) e^{il\Delta z} \\ 2(\cos(k\Delta x) + 2) & 4(\cos(k\Delta x) + 2) e^{il\Delta z} \end{pmatrix}. \quad (41)$$

$$M_w = M_b = Q = \frac{\Delta x \Delta z}{30} \begin{pmatrix} (8 - 2 \cos(l\Delta z)) e^{ik\Delta x/2} & 4 \cos\left(\frac{l\Delta z}{2}\right) e^{ik\Delta x/2} \\ (2e^{il\Delta z} + 2) e^{ik\Delta x/2} & 16 e^{ik\Delta x/2} e^{il\Delta z/2} \end{pmatrix}. \quad (42)$$

$$M_p = \frac{\Delta x \Delta z}{6} \begin{pmatrix} 2 e^{ik\Delta x/2} & e^{ik\Delta x/2} e^{il\Delta z} \\ e^{ik\Delta x/2} & 2 e^{ik\Delta x/2} e^{il\Delta z} \end{pmatrix}. \quad (43)$$

$$D_x^u = \frac{\Delta z}{6} \begin{pmatrix} 4 i \sin\left(\frac{k\Delta x}{2}\right) & 2 i \sin\left(\frac{k\Delta x}{2}\right) e^{il\Delta z} \\ 2 i \sin\left(\frac{k\Delta x}{2}\right) & 4 i \sin\left(\frac{k\Delta x}{2}\right) e^{il\Delta z} \end{pmatrix}. \quad (44)$$

Table 4: Global error measured for the acoustic mode, each case has the normalised L_2 error is calculated, as well as the maximum and minimum error. The higher-order cases perform better overall, however, have larger maximum errors.

case	Normalised L_2 error norm	Max error	Min Error
(0, 0)	0.000482784	0.0404953	2.08984e-09
(0, 1)	0.000465869	0.0824462	3.2898e-10
(1, 0)	0.000465834	0.0824227	9.60074e-10
(1, 1)	0.000400848	0.0826268	8.27239e-11

$$D_x^p = \frac{\Delta z}{6} \begin{pmatrix} 2(e^{ik\Delta x} - 1) & (e^{ik\Delta x} - 1)e^{il\Delta z} \\ (e^{ik\Delta x} - 1) & 2(e^{ik\Delta x} - 1)e^{il\Delta z} \end{pmatrix}. \quad (45)$$

$$D_z^w = \frac{\Delta x}{6} \begin{pmatrix} (5 - e^{-il\Delta z})e^{ik\Delta x/2} & (e^{il\Delta z} - 5)e^{ik\Delta x/2} \\ -4e^{ik\Delta x/2} & 4e^{ik\Delta x/2}e^{il\Delta z} \end{pmatrix}. \quad (46)$$

$$D_z^p = \frac{\Delta x}{6} \begin{pmatrix} (e^{il\Delta z} - 5)e^{ik\Delta x/2} & 4e^{ik\Delta x/2}e^{il\Delta z/2} \\ (5e^{il\Delta z} - 1)e^{ik\Delta x/2} & -4e^{ik\Delta x/2}e^{il\Delta z/2} \end{pmatrix}. \quad (47)$$

C Acoustic mode statistics

Details of the error statistics for the acoustic mode can be found in table (4).

D Timestep pseudocode

Pseudocode for the timestep procedure is found in section [D](#)

E Test case resolutions

As mentioned in section [7](#), we ensure that in each test case the average distance between DoFs is roughly kept the same. Table [5](#) details the horizontal and vertical resolutions for each test case and each order.

Algorithm 1 Pseudocode of a single Semi-Implicit Quasi-Newton time step, the initial state is given as X^0 with k_{\max} and I_{\max} being the number of outer and inner loops, respectively.

```

1: Set:  $X^{n+1} \leftarrow X^n$ 
2: Explicit forcing:  $X_f \leftarrow X^n + (1 - \alpha)\Delta t F(X^n)$ 
3:  $k \leftarrow 0$ 
4: Outer loop
5: while  $k < k_{\max}$  do:
6:   Update advecting velocity:  $\bar{\mathbf{u}} \leftarrow \frac{1}{2}(\mathbf{u}^{n+1} + \mathbf{u}^n)$ 
7:   Advect state:  $X_a \leftarrow A_{\bar{\mathbf{u}}}(X_f)$ 
8:    $i \leftarrow 0$ 
9:   Inner loop
10:  while  $i < I_{\max}$  do
11:    Implicit forcing:  $X_f \leftarrow X_a + \alpha\Delta t F(X^n)$ 
12:    Calculate residual:  $X_r \leftarrow X_f - X^{n+1}$ 
13:    Solve:  $S(\Delta X) = X_r$  for  $\Delta X$ 
14:    Increment  $X^{n+1} \leftarrow X^{n+1} + \Delta X$ 
15:     $i \leftarrow i + 1$ 
16:  end while
17:   $k \leftarrow k + 1$ 
18: end while
19: Advance time step:  $X^n \leftarrow X^{n+1}$ 

```

Test Case	(0, 0)	(0, 1)	(1, 0)	(1, 1)
Gravity wave	(1000m, 1000m)	(1000m, 2000m)	(2000m, 1000m)	(2000m, 2000m)
Travelling vortex	(100m, 100m)	(100m, 200m)	(200m, 100m)	(200m, 200m)
Schär Wave	(500m, 300m)	(500m, 600m)	(1000m, 300m)	(1000m, 600m)

Table 5: Reference table for resolutions of idealised test cases for the different order cases

References

- Adams SV, Ford RW, Hambley M, Hobson JM, Kavčič I, Maynard CM, Melvin T, Müller EH, Mullerworth S, Porter AR, Rezny M, Shipway BJ, Wong R. 2019. LFRic: Meeting the challenges of scalability and performance portability in Weather and Climate models. *Journal of Parallel and Distributed Computing* **132**: 383–396, doi:10.1016/j.jpdc.2019.02.007.
- Arakawa AKIO, Lamb VR. 1977. Computational Design of the Basic Dynamical Processes of the UCLA General Circulation Model. In: *Methods in Computational Physics: Advances in Research and Applications, General Circulation Models of the Atmosphere*, vol. 17, Chang JULIUS (ed), Elsevier, pp. 173–265, doi:10.1016/B978-0-12-460817-7.50009-4.
- Arnold DN, Falk RS, Winther R. 2006. Differential Complexes and Stability of Finite Element Methods I. The de Rham Complex. In: *Compatible Spatial Discretizations*, vol. 142, Arnold DN, Bochev PB, Lehoucq RB, Nicolaidis RA, Shashkov M (eds), Springer New York: New York, NY, ISBN 978-0-387-30916-3, pp. 23–46, doi:10.1007/0-387-38034-5_2.
- Benacchio T, Wood N. 2016. Semi-implicit semi-Lagrangian modelling of the atmosphere: a Met Office perspective. *Communications in Applied and Industrial Mathematics* **7**(3): 4–25, doi:10.1515/caim-2016-0020, URL <https://reference-global.com/article/10.1515/caim-2016-0020>.
- Bendall TM, Cotter CJ, Shipton J. 2019. The Recovered Space Advection Scheme for Lowest-Order Compatible Finite Element Methods. *Journal of Computational Physics* **390**: 342–358, doi:10.1016/j.jcp.2019.04.013.
- Bendall TM, Wimmer GA. 2023. Improving the accuracy of discretisations of the vector transport equation on the lowest-order quadrilateral Raviart-Thomas finite elements. *Journal of Computational Physics* **474**: 111 834, doi:10.1016/j.jcp.2022.111834.
- Bendall TM, Wood N, Thuburn J, Cotter CJ. 2023. A solution to the trilemma of the moist Charney–Phillips staggering. *Quarterly Journal of the Royal Meteorological Society* **149**(750): 262–276, doi:10.1002/qj.4406.
- Burgess BH, Erler AR, Shepherd TG. 2013. The Troposphere-to-Stratosphere Transition in Kinetic Energy Spectra and Nonlinear Spectral Fluxes as Seen in ECMWF Analyses. *Journal of the Atmospheric Sciences* **70**(2): 669–687, doi:10.1175/JAS-D-12-0129.1, URL <https://journals.ametsoc.org/view/journals/atsc/70/2/jas-d-12-0129.1.xml>.

- Charney JG, Phillips NA. 1953. NUMERICAL INTEGRATION OF THE QUASI-GEOSTROPHIC EQUATIONS FOR BAROTROPIC AND SIMPLE BAROCLINIC FLOWS. *Journal of the Atmospheric Sciences* **10**(2): 71–99, doi:10.1175/1520-0469(1953)010<0071:NIOTQG>2.0.CO;2.
- Chew R, Benacchio T, Hastermann G, Klein R. 2021. A one-step blended soundproof-compressible model with balanced data assimilation: theory and idealised tests. doi:10.1175/MWR-D-21-0175.1, URL <https://arxiv.org/abs/2103.11861v2>.
- Cotter CJ. 2023. Compatible finite element methods for geophysical fluid dynamics. doi:10.48550/arXiv.2302.13337.
- Cotter CJ, Shipton J. 2012. Mixed finite elements for numerical weather prediction. *Journal of Computational Physics* **231**(21): 7076–7091, doi:10.1016/j.jcp.2012.05.020.
- Cotter CJ, Shipton J. 2022. A compatible finite element discretisation for the nonhydrostatic vertical slice equations. <http://arxiv.org/abs/2210.07861>, doi:10.48550/arXiv.2210.07861.
- Cotter CJ, Thuburn J. 2014. A finite element exterior calculus framework for the rotating shallow-water equations. *1526* doi:10.1016/j.jcp.2013.10.008.
- Durran DR. 2010. *Numerical Methods for Fluid Dynamics, Texts in Applied Mathematics*, vol. 32. Springer: New York, NY, ISBN 978-1-4419-6411-3 978-1-4419-6412-0, doi:10.1007/978-1-4419-6412-0.
- Eldred C, Le Roux DY. 2018. Dispersion analysis of compatible Galerkin schemes for the 1D shallow water model. *Journal of Computational Physics* **371**: 779–800, doi:10.1016/j.jcp.2018.06.007.
- Giraldo FX, de Bragança Alves FAV, Kelly JF, Kang S, Reinecke PA. 2024. A performance study of horizontally explicit vertically implicit (HEVI) time-integrators for non-hydrostatic atmospheric models. *Journal of Computational Physics* **515**: 113275, doi:10.1016/j.jcp.2024.113275.
- Giraldo FX, Restelli M. 2008. A study of spectral element and discontinuous Galerkin methods for the Navier–Stokes equations in nonhydrostatic mesoscale atmospheric modeling: Equation sets and test cases. *Journal of Computational Physics* **227**(8): 3849–3877, doi:10.1016/j.jcp.2007.12.009.
- Guerra JE, Ullrich PA. 2016. A high-order staggered finite-element vertical discretization for non-hydrostatic atmospheric models. *Geoscientific Model Development* **9**(5): 2007–2029, doi:10.5194/gmd-9-2007-2016.

- Ham DA, Kelly PHJ, Mitchell L, Cotter CJ, Kirby RC, Sagiya K, Bouziani N, Vorderwuelbecke S, Gregory TJ, Betteridge J, Shapero DR, Nixon-Hill RW, Ward CJ, Farrell PE, Brubeck PD, Marsden I, Gibson TH, Homolya M, Sun T, McRae ATT, Luporini F, Gregory A, Lange M, Funke SW, Rathgeber F, Bercea GT, Markall GR. 2023. Firedrake user manual. doi:10.25561/104839.
- Hannah WM, Bradley AM, Guba O, Tang Q, Golaz JC, Wolfe J. 2021. Separating Physics and Dynamics Grids for Improved Computational Efficiency in Spectral Element Earth System Models. *Journal of Advances in Modeling Earth Systems* **13**(7): e2020MS002419, doi:10.1029/2020MS002419.
- Hartney N, Bendall TM, Shipton J. 2025. Exploring forms of the moist shallow water equations using a new compatible finite element discretisation. <http://arxiv.org/abs/2409.07182>, doi:10.48550/arXiv.2409.07182.
- Herrington AR, Lauritzen PH, Taylor MA, Goldhaber S, Eaton BE, Bacmeister JT, Reed KA, Ullrich PA. 2019. Physics–Dynamics Coupling with Element-Based High-Order Galerkin Methods: Quasi-Equal-Area Physics Grid. *Monthly Weather Review* doi:10.1175/MWR-D-18-0136.1.
- Izzo G, Jackiewicz Z. 2022. Strong Stability Preserving Runge–Kutta and Linear Multistep Methods. *Bulletin of the Iranian Mathematical Society* **48**(6): 4029–4062, doi:10.1007/s41980-022-00731-x, URL <https://doi.org/10.1007/s41980-022-00731-x>.
- Kadioglu SY, Klein R, Minion ML. 2008. A fourth-order auxiliary variable projection method for zero-Mach number gas dynamics. *Journal of Computational Physics* **227**: 2012–2043, doi:10.1016/j.jcp.2007.10.008.
- Kowalczyk K. 2025. On compatible finite elements for atmosphere modelling doi:10.25560/127314, URL <https://hdl.handle.net/10044/1/127314>.
- Le Roux DY, Rostand V, Pouliot B. 2007. Analysis of Numerically Induced Oscillations in 2D Finite-Element Shallow-Water Models Part I: Inertia-Gravity Waves. *SIAM Journal on Scientific Computing* **29**(1): 331–360, doi:10.1137/060650106.
- Melvin T, Benacchio T, Shipway B, Wood N, Thuburn J, Cotter C. 2019. A mixed finite-element, finite-volume, semi-implicit discretisation for atmospheric dynamics: Cartesian geometry. *Quarterly Journal of the Royal Meteorological Society* **145**: 2835–2853, doi:10.1002/qj.3501.
- Melvin T, Benacchio T, Thuburn J, Cotter C. 2018. Choice of function spaces for thermodynamic variables in mixed finite element methods. *Quarterly Journal of the Royal Meteorological Society* **144**: 900–916, doi:10.1002/qj.3268.

- Melvin T, Dubal M, Wood N, Staniforth A, Zerroukat M. 2010. An inherently mass-conserving iterative semi-implicit semi-Lagrangian discretization of the non-hydrostatic vertical-slice equations. *Quarterly Journal of the Royal Meteorological Society* **136**(648): 799–814, doi:10.1002/qj.603.
- Melvin T, Shipway B, Wood N, Benacchio T, Bendall T, Boutle I, Brown A, Johnson C, Kent J, Pring S, Smith C, Zerroukat M, Cotter C, Thuburn J. 2024. A mixed finite-element, finite-volume, semi-implicit discretisation for atmospheric dynamics: Spherical geometry. *Quarterly Journal of the Royal Meteorological Society* **150**(764): 4252–4269, doi:10.1002/qj.4814.
- Melvin T, Staniforth A, Cotter C. 2014. A two-dimensional mixed finite-element pair on rectangles. *Quarterly Journal of the Royal Meteorological Society* **140**(680): 930–942, doi:10.1002/qj.2189.
- Nair RD, Choi HW, Tufo HM. 2009. Computational aspects of a scalable high-order discontinuous Galerkin atmospheric dynamical core. *Computers & Fluids* **38**(2): 309–319, doi:10.1016/j.compfluid.2008.04.006.
- Natale A, Shipton J, Cotter CJ. 2016. Compatible finite element spaces for geophysical fluid dynamics. *Dynamics and Statistics of the Climate System* **1**(1): dzw005, doi:10.1093/climsys/dzw005.
- Schär C, Leuenberger D, Fuhrer O, Lüthi D, Girard C. 2002. A New Terrain-Following Vertical Coordinate Formulation for Atmospheric Prediction Models. *American Meteorological Society* **130**(10): 2459–2480.
- Schmidt H, Rast S, Bao J, Cassim A, Fang SW, Jimenez-de la Cuesta D, Keil P, Kluft L, Kroll C, Lang T, Niemeier U, Schneidereit A, Williams AIL, Stevens B. 2024. Effects of vertical grid spacing on the climate simulated in the ICON-Sapphire global storm-resolving model. *Geoscientific Model Development* **17**(4): 1563–1584, doi:10.5194/gmd-17-1563-2024.
- Skamarock WC, Klemp JB. 1994. Efficiency and Accuracy of the Klemp-Wilhelmson Time-Splitting Technique. *Monthly Weather Review* **122**(11): 2623–2630, doi:10.1175/1520-0493(1994)122<2623:EAAOTK>2.0.CO;2.
- Skamarock WC, Ong H, Klemp JB. 2021. A Fully Compressible Nonhydrostatic Deep-Atmosphere Equations Solver for MPAS. *Monthly Weather Review* **149**(2): 571–583, doi:10.1175/MWR-D-20-0286.1, URL <https://journals.ametsoc.org/view/journals/mwre/149/2/MWR-D-20-0286.1.xml>.
- Skamarock WC, Snyder C, Klemp JB, Park SH. 2019. Vertical Resolution Requirements in Atmo-

spheric Simulation. *Monthly Weather Review* **147**(7): 2641–2656, doi:10.1175/MWR-D-19-0043.1, URL <https://journals.ametsoc.org/view/journals/mwre/147/7/mwr-d-19-0043.1.xml>.

Staniforth A, Thuburn J. 2012. Horizontal grids for global weather and climate prediction models: A review: Horizontal Grids for Global Models: A Review. *Quarterly Journal of the Royal Meteorological Society* **138**(662): 1–26, doi:10.1002/qj.958.

Ullrich PA, Melvin T, Jablonowski C, Staniforth A. 2014. A proposed baroclinic wave test case for deep- and shallow-atmosphere dynamical cores. *Quarterly Journal of the Royal Meteorological Society* **140**(682): 1590–1602, doi:10.1002/qj.2241.

Waite ML, Snyder C. 2009. The Mesoscale Kinetic Energy Spectrum of a Baroclinic Life Cycle. *Journal of the Atmospheric Sciences* **66**(4): 883–901, doi:10.1175/2008JAS2829.1, URL <https://journals.ametsoc.org/view/journals/atsc/66/4/2008jas2829.1.xml>.

Wood N, Staniforth A, White A, Allen T, Diamantakis M, Gross M, Melvin T, Smith C, Vosper S, Zerroukat M, Thuburn J. 2014. An inherently mass-conserving semi-implicit semi-Lagrangian discretization of the deep-atmosphere global non-hydrostatic equations. *Quarterly Journal of the Royal Meteorological Society* **140**(682): 1505–1520, doi:10.1002/qj.2235.